The dual-port splitter with >48% efficiency in ±1st diffraction orders

JIAQI LI, JIAMING REN, WENKUN PENG, PEIHONG ZENG, YUSEN HUANG, YUQING XIAO, JINJIE LI, HONGWEI ZHAN, BO WANG*, QU WANG, FANGTENG ZHANG
Guangdong University of Technology, Guangzhou 510006, China

A novel reflective grating with a sandwiched structure is proposed. Under the normal incidence, the grating can function as a dual-port beam splitter. Rigorous coupled-wave analysis (RCWA) is used to optimize the grating for high efficiency. Based on the optimized parameters, high efficiency of the ±1st orders of 48.17% for transverse electric (TE) polarization and 48.19% for transverse magnetic (TM) polarization can be achieved, where the 0th order is less than 0.99% for TE and TM polarizations, and the total efficiency can reach 98%. Simultaneously, we effectively analyzed and verified the device data using simplified modal method (SMM), finite element method (FEM), and electric field distribution. In addition, the proposed grating also has a good performance at a bandwidth of 64 nm and the duty cycle of 0.668-0.732.

(Received January 14, 2025; accepted October 10, 2025)

Keywords: Subwavelength grating, Multilayer structure, Normal incidence, Dual-port splitter

1. Introduction

Due to the novel diffraction properties, the grating with a periodic structure has always been the focus of optical research [1-7]. The optical field for the electromagnetic wave can be adjusted by the metasurfaces [8, 9]. High-efficiency gratings are key elements in various optical systems, for example, photodetectors [10-12], sensors [13-15], absorbers [16-18], etc. With the development of modern optical system, the demand for grating with high integration and diffraction efficiency is increasing. With the improvement of micro-nano processing technology, there is more promotion for the optical devices design and performance [19]. Compared to the past, the grating density has become increasingly high, and the diffraction properties of high-density grating are different from low-density grating. Wang et al. described a novel reflection-reduced two-layer grating. For the TE and TM polarizations, the efficiencies of 99.69% and 99.64% can be achieved, respectively [20]. Feng et al. presented a dual-function subwavelength fused-silica grating which can work as a polarization-selective beam splitter with a total efficiency of 98% for TM polarization and a high-efficiency grating with the efficiency of the -1st order of 95% for TE polarization [21].

The analysis methods of grating can be divided into scalar diffraction theory [22, 23] and vector diffraction theory [24, 25]. For subwavelength grating [26], where the grating period is close to the wavelength (resonance regime), its polarization characteristic becomes very pronounced. Scalar diffraction theory can no longer be used to calculate diffraction efficiency. Therefore, vector diffraction theory should be employed for subwavelength grating analysis, including RCWA [27-29], FEM [30], and finite-difference time-domain method (FDTD) [31].

In this paper, we propose a sandwiched reflective grating structure, which can function as a dual-port beam splitter [32, 33]. One of the vector diffraction theories, RCWA, divides the grating structure into an incident region, a grating region, and an output region. By employing Fourier series, Maxwell's equations, and boundary conditions, the electric field distribution throughout the entire space can be accurately obtained [34-36]. Therefore, we adopted RCWA for theoretical analysis of the optical performance of this beam splitter. Through RCWA calculations and optimization, we obtained optimal parameters for this dual-port beam splitter structure under both TE and TM polarizations. The results indicate that when incident light with a wavelength of 1.550 μm is vertically incident on the grating layer along the normal direction of the fused silica surface, the diffraction efficiencies for both ±1st orders exceed 48% under dual polarization, while effectively suppressing the 0th-order diffraction efficiency. Additionally, due to the incident angle and grating structure design, the incident energy is evenly coupled into the +1st and -1st diffraction orders. In Section III of this paper, we provide a detailed analysis of the diffraction states using SMM. Subsequently, we validated the performance of the beam splitter through electric field distribution and FEM. What's more, this

paper also discusses the bandwidth of incident wavelength and the tolerance of duty cycle of grating in actual fabrication.

2. Structure and numerical calculations

As shown in Fig. 1, The grating structure consists of, from bottom to top, the metal layer, the connecting-layer, the periodic grating ridges and the capping layer. The grating grooves filled with air (n=1.00) are positioned between grating ridges. Fused silica is used as the material for grating substrate, connecting layer and grating ridge. Due to the advantages of appropriate price and strong plasticity of metal silver, it is reasonable to choose it to be the reflective layer whose thickness is h_m= 0.100 μm and its refractive index n_m=0.469-i*9.32. Secondly, the depth of grating groove is defined as h_1. The thicknesses of connecting-layer and metal layer are h_2 and h_m, respectively. The grating period is defined as d, and the width of grating ridge is a, so the duty cycle is $f=a/d$. In this work, the normal incident wave with wavelength of λ=1.550 μm illuminates the grating from fused-silica, so the refractive index of the incident region is n_1=1.45. Due to the refraction of metal layer, the exit region is also fused silica with the refractive index n_1.

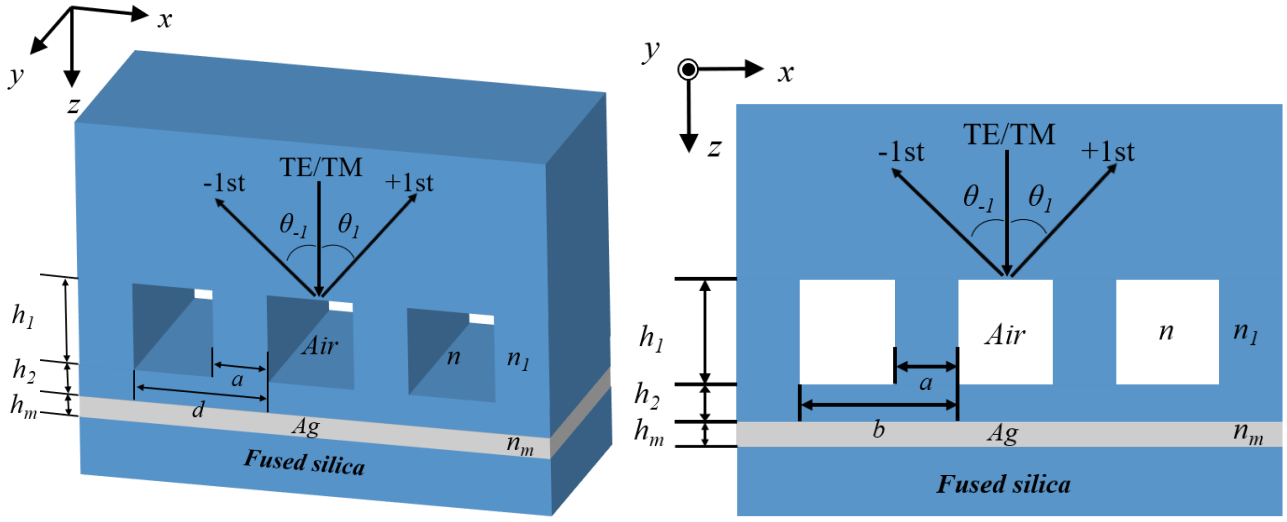

(a) (b)

Fig. 1. Schematic diagram of dual -port grating with a sandwiched structure: (a) 3-D view (b) 2-D view (colour online)

The performance of a grating depends on its structural parameters. To achieve a high-efficiency grating with dual-port functionality and suppression of the 0th-order diffraction, we employed RCWA to optimize the grating structure. Through RCWA simulations, the optimal structural parameters were obtained: the period d=2.100 μm, the duty cycle f=0.7, the thicknesses h_1, h_2 and h_m of 2.000 μm, 1.850 μm and 0.100 μm, respectively. The parameters are listed in Table 1. Through numerical calculations, as shown in Fig. 2, high efficiencies of 48.17% for TE polarization and 48.19% for TM polarization are achieved in the ±1st orders. The 0th-order efficiency remains below 0.99% for both polarizations, while the total efficiency exceeds 98%.

Table 1. The optimized parameters of grating structure

f	d	h_1	h_2	h_m
0.7	2.100 μm	2.000 μm	1.850 μm	0.100 μm

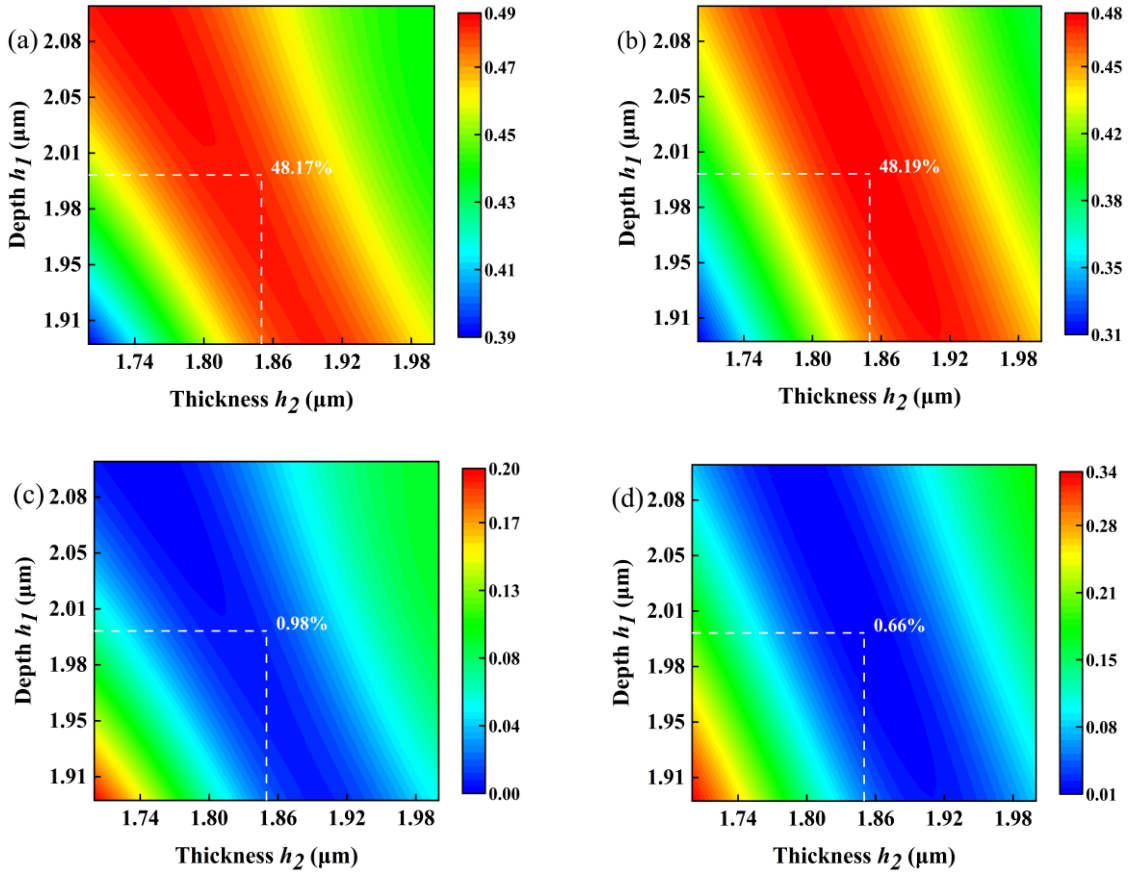

Fig. 2. The efficiency versus the thickness of grating groove depth and connecting layer under normal incidence with λ=1.550 μm, d=2.100 μm, h_m=0.100 μm and f=0.7: (a) ±1st orders of TE polarization; (b) ±1st orders of TM polarization; (c) 0th order of TE polarization; (d) 0th order of TM polarization (colour online)

The above structure is theoretically designed, and due to the involvement of a silver reflective layer and relatively deep etching, it is necessary to discuss the feasibility of the fabrication process for this device structure. The manufacturing steps are as follows [37,38]: First, we prepare a layer of fused quartz as the substrate and deposit a metallic silver layer using magnetron sputtering technology. Second, the grating structure is obtained by coating photoresist on the quartz surface, followed by exposure, development, patterning, and ion beam etching techniques. The grating is then subjected to plasma activation treatment. Finally, a similarly plasma-activated fused quartz substrate is placed over the grating, and the sandwich-structured grating is bonded firmly with the metal silver layer. Compared to traditional surface gratings, the sandwich-structured grating with a cover layer reduces Fresnel losses. This further validates the high credibility of the structure investigated in this study.

3. SMM for the grating structures

In this study, the performance of the dual-port beam splitter primarily relies on simulation results. It is necessary to explore the underlying physical mechanisms behind it. Since RCWA cannot describe the energy exchange between diffraction orders within the grating structure, we employ SMM for theoretical analysis of its fundamental physical principles. According to SMM, the characteristic functions of TE-polarized and TM-polarized incident light in the grating region are respectively [39,40]:

$$F\left(n_{eff}^2\right) = \cos(\beta f d)\cos[\gamma(1-f)d] - \frac{\beta^2+\gamma^2}{2\beta\gamma} sin(\beta f d)\, sin[\gamma(1-f)d], \quad (1)$$

$$F\left(n_{eff}^2\right) = \cos(\beta f d)\cos[\gamma(1-f)d] - \frac{n_g^4\beta^2+n_r^4\gamma^2}{2n_g^4 n_r^4\beta\gamma} sin(\beta f d)\, sin[\gamma(1-f)d], \quad (2)$$

$$\beta = \frac{2\pi\sqrt{n_r^2-n_{eff}^2}}{\lambda}, \gamma = \frac{2\pi\sqrt{n_g^2-n_{eff}^2}}{\lambda} \quad (3)$$

where, n_{eff} represents the effective refractive index of the excited discrete modes. f and d represent the duty

cycle and grating period, respectively. n_r and n_g represent the refractive indices of the grating ridge and grating groove, respectively. This structural design employs normal incidence, so the self-collimating line $F(n_{eff}^2) = 1$. When incident light propagates along the grating, it excites discrete modes within the grating layer. The properties of these discrete modes depend on the effective refractive index. When $n_{eff}^2 > 0$, the effective refractive index of the discrete mode is a positive real number, allowing the light to penetrate and transmit through the grating. When $n_{eff}^2 < 0$, the effective refractive index of the discrete mode is imaginary, causing the incident light to decay rapidly during propagation along the grating [41]. Therefore, this case is not considered in this study. The relationship between the grating characteristic function and the effective refractive index is shown in Fig. 3. It can be observed that the discrete modes excited by TE-polarized and TM-polarized light within the grating are the 0th mode, 1st mode, and 2nd mode. Their corresponding effective refractive indices are listed in Table 2(a).

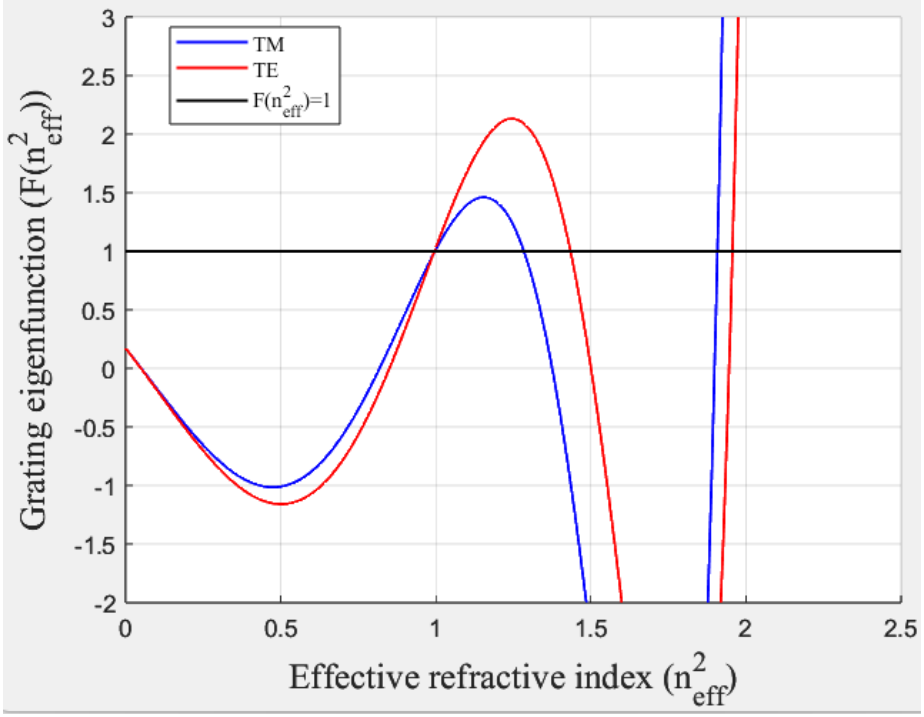

Fig. 3. The relationship curve between the effective refractive index and the grating characteristic function (colour online)

Table 2. Simplified modal method for the dual-port functional gratings

(a) Effective refractive index of the grating layer.

	n_{0eff}	n_{1eff}	n_{2eff}
TE	1.3987	1.1975	0.9975
TM	1.3813	1.1331	0.9983

(b) The energy exchange between the grating modes and the diffraction orders

Mode	*Diffraction Order*			
	TE (0th)	*TE (±1st)*	*TM (0th)*	*TM (±1st)*
Mode 0	0.8415	0.0785	0.7585	0.1203
Mode 1	0	0.4919	0	0.4676
Mode 2	0.1376	0.3930	0.1371	0.3933

During the process of incident light penetrating the grating layer, it undergoes two coupling events. The incident light couples with the grating for the first time, exciting the grating mode; the second coupling occurs between the grating mode and the diffraction orders, and the energy exchange between them can be described by the following formula [42,43].

$$\langle E_{yj}(x) \leftrightarrow u_m \rangle = \frac{\left|\int_0^d E_{yj}(x)u_m(x)dx\right|^2}{\int_0^d |E_{yj}(x)|^2 dx \int_0^d |u_m(x)|^2 dx}, \quad (4)$$

$$\langle H_{yk}(x) \leftrightarrow u_q \rangle = \frac{\left|\int_0^d H_{yk}(x)u_q(x)dx\right|^2}{\int_0^d |H_{yk}(x)|^2 dx \int_0^d |u_q(x)|^2 dx} \quad (5)$$

Here, $E_{yj}(x)$ and u_m denote the diffraction order and grating mode for TE polarization, respectively.

$H_{yk}(x)$ and u_q denote the diffraction order and grating mode for TM polarization, respectively. Using formulas 4 and 5, the weight for energy exchange between grating modes and diffraction orders within this dual-port beam splitter grating layer can be calculated, as detailed in Table 2(b). Analysis based on the SMM theory, combined with the aforementioned chart data, can effectively explain that our proposed dual-port beam splitter exhibits high diffraction efficiency in the ±1st diffraction orders and incorporates a 0th-order diffraction suppression capability.

4. Discussion and data analysis

Based on the theoretical parameters calculated via RCWA, we performed analysis and validation using the FEM. Table 3 lists the calculation results from both methods. It can be seen that the FEM results are almost identical to the RCWA results, thus effectively demonstrating the credibility of the theoretical parameters for this device.

Table 3. The efficiencies of grating under the optimized parameters based on RCWA and FEM

Theory	$\eta_{\pm 1}{}^{TE}$ (%)	$\eta_{\pm 1}{}^{TM}$ (%)	$\eta_0{}^{TE}$ (%)	$\eta_0{}^{TM}$ (%)
RCWA	48.17	48.19	0.98	0.66
FEM	48.12	48.17	0.92	0.65

Fig. 4 displays the normalized electric field distribution. Evidently, when h_m is 0.100 μm, the energy of both TE and TM polarizations reaching the metal layer is almost entirely reflected back and symmetrically distributed across the grating, the cover layer, and the connection layer. Notably, this energy distribution further demonstrates that the ±1st diffraction orders exhibit identical diffraction efficiency. Additionally, the electric field energy distribution differs significantly between TE and TM polarizations within the grating layer. Under TE polarization, the electric field energy is primarily concentrated in the grating ridges, whereas under TM polarization, it predominantly localizes within the grating trenches.

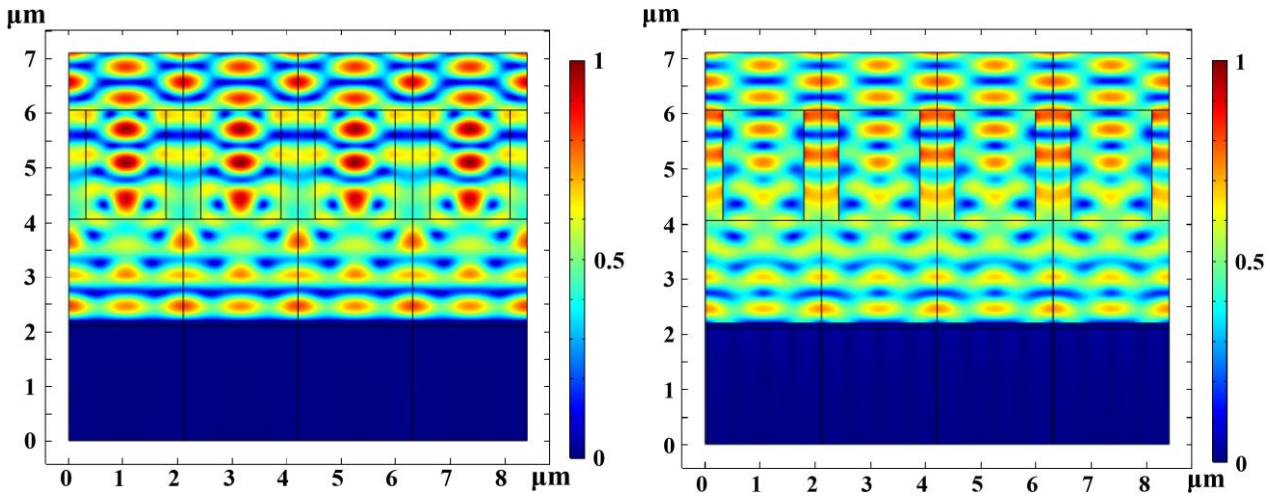

(a) (b)

Fig. 4. The normalized electric field distribution diagram of the grating with λ=1.550 μm, d=2.100 μm, h_m=0.100 μm and f=0.7: (a) TE polarization; (b) TM polarization (colour online)

Furthermore, to highlight the distinctive features of the structure investigated in this study compared to other relevant reports [44,45], we compare the diffraction order efficiency, structure, polarization compatibility, and fabrication tolerance. As shown in Table 4, we find that, compared to the other two structures, the proposed design in this study demonstrates significant advantages in incident wavelength bandwidth and duty cycle tolerance, thereby better meeting practical manufacturing requirements. Compared to the Ref. [45], the diffraction efficiencies for both the +1st and -1st orders under TE and TM polarizations have been improved in this work. Furthermore, compared to the Ref. [44], the diffraction efficiencies for the ±1st orders under TM polarization have been significantly improved, and the suppression of the 0th-order diffraction efficiency has also been further strengthened. Interestingly, compared to beam-splitting gratings limited to a specific polarization, polarization-independent dual-port beam splitters demonstrate promising application potential in laser beam processing or transient grating spectroscopy (TGS) [46,47]. For instance, TGS based on polarization -

insensitive diffraction gratings can be employed to investigate the distribution of the mean free path of energy carriers [47]. Detailed comparisons are presented in Table 4.

Table 4. The comparison of the structural data proposed in this work with the structural data from other relevant studies

Scheme	*Ref. [44]*	*Ref. [45]*	*This work*
η_0^{TE} (%)	0.25	0.51	0.98
$\eta_{\pm 1}^{TE}$ (%)	48.63	48.01	48.17
η_0^{TM} (%)	2.90	0.85	0.66
$\eta_{\pm 1}^{TM}$ (%)	44.30	47.90	48.19
Covering layer	Yes	No	Yes
Reflective layer	No	Yes	Yes
Connecting layer	Yes	Yes	Yes
Polarization state	Polarization independent	Polarization independent	Polarization independent
Bandwidth of wavelength	38 nm ($\eta_{\pm 1}$>42%)	20 nm ($\eta_{\pm 1}$>47%)	64 nm ($\eta_{\pm 1}$>47%)
Duty cycle tolerance	0.09 ($\eta_{\pm 1}$>42%)	0.03 ($\eta_{\pm 1}$>47%)	0.064 ($\eta_{\pm 1}$>47%)

The selection of duty cycle and grating trench depth critically governs the diffraction efficiency of the grating. The trench depth controls the phase accumulation of incident light within the grating, serving as a phase modulation mechanism. Insufficient depth leads to inadequate phase modulation, whereas excessive depth causes energy leakage to non-target diffraction orders. Meanwhile, the duty cycle, defined as the ratio of the grating ridge width to the period, influences the distribution of diffraction efficiency across different orders. Furthermore, when the grating layer directly contacts the metal reflective layer, light induces the skin effect at the metal surface, increasing propagation loss. By introducing a connection layer, the propagation phase difference accumulates to achieve reflective phase compensation, thereby enhancing the efficiency of specific diffraction orders and broadband performance. Fig. 5 shows the efficiency versus the thickness h_2 under the normal incidence. In Fig. 5, when h_2 is 1.850 μm, the function of the grating is well realized.

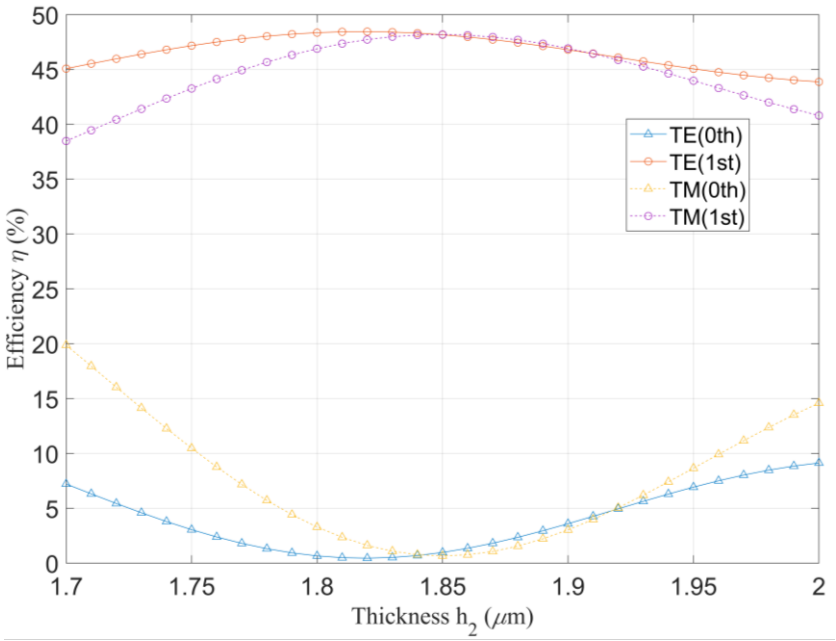

Fig. 5. The efficiency versus the thickness h_2 of connecting layer under normal incidence with λ=1.550 μm, d=2.100 μm, h_m=0.100 μm and f=0.7 (colour online)

It is necessary to consider the cost of grating fabrication. Fig. 6 presents the efficiency versus the metal layer thickness h_m. When h_m is from 0 μm to 0.100 μm, the grating reflection efficiency increases; When h_m is 0.100 μm, the efficiency reaches the maximum; When h_m is greater than 0.100 μm, the efficiency is hardly changing. Therefore, it is reasonable to choose h_m as 0.100 μm.

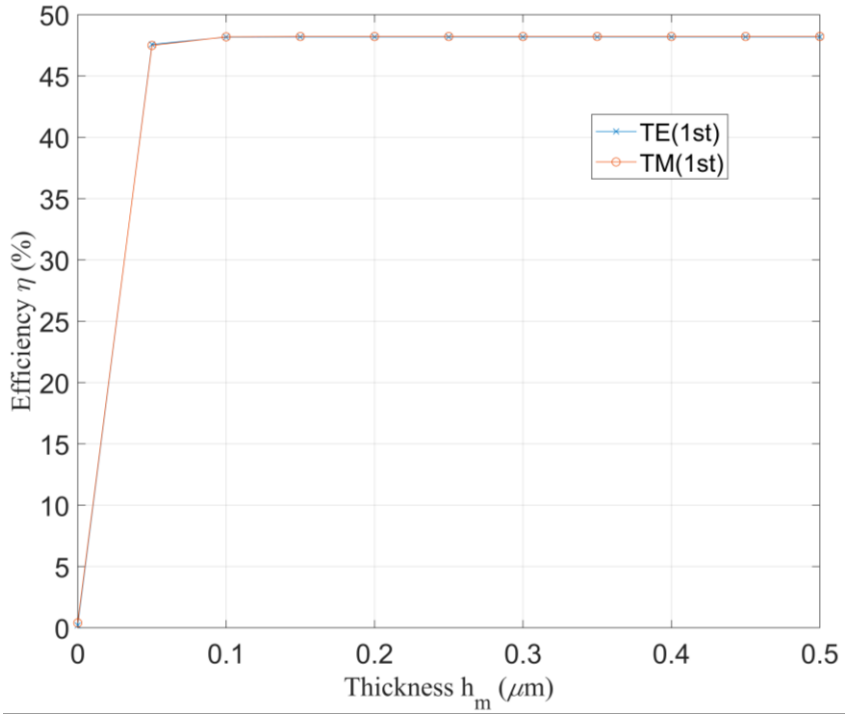

Fig. 6. The relationship between the efficiency and the thickness of metal layer (colour online)

In this work, the designed structure operates under normal incidence at a theoretical wavelength of λ=1550 nm to achieve high diffraction efficiency in the ±1st orders. However, in practical applications, the incident wavelength cannot be precisely fixed at 1550 nm, which requires investigation into its performance across a range of incident wavelengths. Fig. 7 shows the efficiency versus the incident wavelength λ. For TE polarization and TM polarization, the ±1-order diffraction efficiencies exceed 47%, while the 0th-order efficiencies are suppressed below 3% over the 64-nm bandwidth spanning 1524 nm to 1588 nm. It indicates that the grating has a wide incident wavelength bandwidth so that it can satisfy the application requirements for wide incident bandwidth.

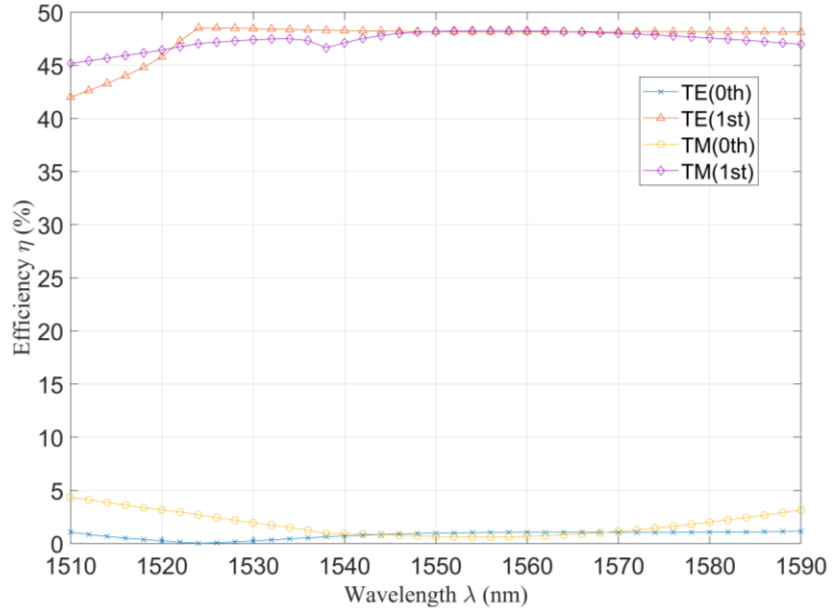

Fig. 7. The efficiency versus the incident wavelength λ with d=2.100 μm, h_1=2.000 μm, h_2=1.850 μm, h_m=0.100 μm and f=0.7 (colour online)

The grating duty cycle in this device is a parameter calculated based on RCWA theory. However, during actual fabrication, limitations in microfabrication precision and process control may lead to deviations in grating etching depth, consequently affecting device performance. It is therefore imperative to systematically investigate the impact of varying grating duty cycles on device performance. Fig. 8 shows the relationship between duty cycle *f* and the grating efficiency. It can be observed that when the duty cycle *f* is within the range of 0.668-0.732, for both polarizations, the efficiencies of the ±1st orders are nearly greater than 47%, and those of 0th order are less than 3.7%. All in all, the grating has a wide incident bandwidth and a large process tolerance in the duty cycle, which is of great significance for the actual production.

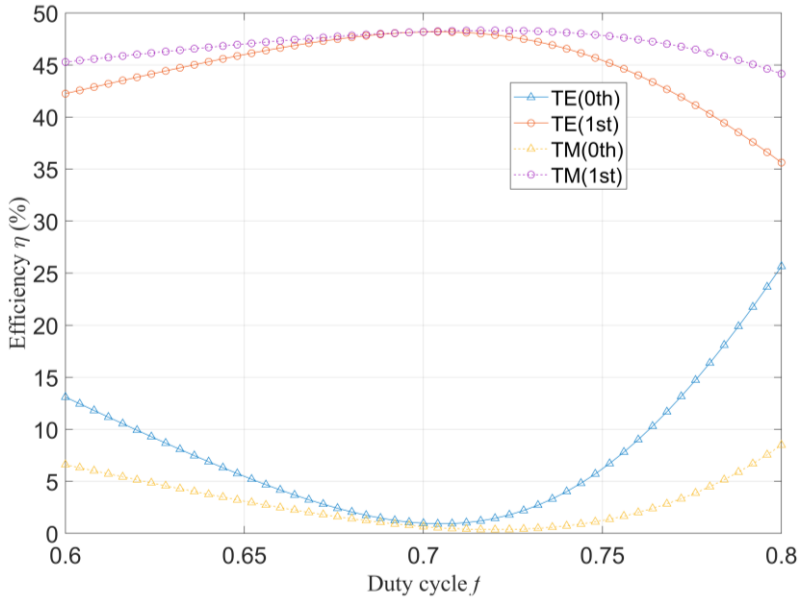

Fig. 8. The relationship between duty cycle f and the grating efficiency with λ=1.550 μm, d=2.100 μm h_1=2.000 μm, h_2=1.850 μm, and h_m=0.100 μm (colour online)

5. Conclusion

In conclusion, this paper proposes an efficient sandwich-structured grating capable of functioning as a dual-port output energy splitter under normal incidence. To enhance efficiency, the structural parameters of the grating were optimized using RCWA. Based on the optimized parameters, the ±1st-order efficiencies of 48.17% for TE polarization and 48.19% for TM polarization were achieved, respectively, while effectively suppressing the 0th-order. The total efficiency can reach 98%. Furthermore, we comprehensively analyzed the physical mechanisms governing the performance of this beam splitter through SMM, FEM simulations, and electric field distributions. The grating can retain high-efficiency in the range of 1524-1588 nm (bandwidth 64 nm). The efficiencies of the ±1st orders are greater than 47% for two polarizations when the duty cycle *f* is within the range of 0.668-0.732. Such a high-efficiency, wide incident bandwidth and wide fabrication tolerance grating should be promising in various optical applications.

Acknowledgements

This work is supported by the Natural Science Foundation of Guangdong Province (2024A1515012690, 2024A1515010109).

References

[1] D. Yan, Y. Qiu, C. Zhao, X. Li, L. Zhang, J. Li, Diam. Relat. Mater. **142**, 110818 (2024).
[2] R. Zhao, L. Su, T. Wang, D. Cong, S. Wang, Y. Gao, Diam. Relat. Mater. **149**, 111581 (2024).
[3] M. Manuvinakurake, U. Gandhi, U. Mangalanathan, S. Sebastian, A. Sundarrajan, D. Yadav, M. Nayak, J. Optoelectron. Adv. M. **23**(3-4), 134-144 (2021).
[4] K. Chakrabarty, P. A. Baker, S. A. Catledge, Diam. Relat. Mater. **147**, 111370 (2024).
[5] J. Zhang, H. Zhang, G. Zhang, Front. Phys. **9**(2), 23204 (2024).
[6] Z. Zhang, S. Yang, Q. Sun, J. Chen, C. Lv, Y. Zhang, J. Zhang, Plasmonics **20**(1), 83 (2025).

[7] B. Li, M. Liu, L. Zeng, X. Zhang, Y. Wei, R. Wen, C. Deng, Diam. Relat. Mater. **146**, 111166 (2024).
[8] H. Han, J. Zhao, W. Zhai, Z. Xiong, D. Niyato, M. D. Renzo, Q.-V. Pham, W. Lu, K.-Y. Lam, IEEE Trans. Commun. **69**(11), 7821 (2021).
[9] Q. Wang, C. Li, B. Fang, L. Ke, J. Lu, X. Ma, Z. Hong, X. Jing, J. Lightw. Technol. **41**(23), 7098 (2023).
[10] A. K. Sharma, A. K. Pandey, J. Phys. D-Appl. Phys. **53**(17), 175103 (2020).
[11] Z. Ma, P. Tang, J. Xue, J. Zhou, Plasmonics **18**(4), 1571 (2023).
[12] S. Kour, S. Das, J. Singh, S. D. Gupta, Plasmonics **20**(3), 1395 (2025).
[13] T. Alwin, Opt. Quantum Electron. **53**(2), 107 (2021).
[14] H. Sarafraz, M. Noori, Plasmonics **20**(7), 5187 (2025).
[15] A. G. Leal-Junior, C. Marques, IEEE Sensors Journal **21**(11), 12719 (2021)
[16] F. Saeed, T. Iqbal, N. Al-Zaqri, I. Warad, M. S. Sultan, Plasmonics **18**(3), 1117 (2023).
[17] A. Afroozeh, Plasmonics **19**(5), 2371 (2024).
[18] S. Ahsan, T. Iqbal, S. Afsheen, M. I. Khan, K. N. Riaz, M. Yousaf, K. Iqbal, A. A. Alobaid, I. Warad, Plasmonics **20**(1), 325 (2025)
[19] Z. Hao, H. Chen, Y. Yin, C.-W. Qiu, S. Zhu, H. Chen, Front. Phys. **19**(4), 42202 (2024).
[20] B. Wang, W. Shu, L. Chen, L. Lei, J. Zhou, IEEE Photon. Technol. Lett. **26**(5), 501 (2014).
[21] J. Feng, C. Zhou, J. Zheng, H. Cao, P. Lv, Appl. Opt. **48**(14), 2697 (2009).
[22] W.-Y. Choi, C.-J. Lee, B.-S. Kim, K.-J. Oh, K. Hong, H.-G. Choo, J. Park, S.-Y. Lee, Appl. Opt. **60**(4), A54 (2021).
[23] C. K. Madsen, Appl. Opt. **60**(9), 2695 (2021).
[24] Z. Zhang, Y. Dai, C. Ma, Opt. Commun. **500**, 127323 (2021).
[25] L. Guo, J. Wang, Optik **157**, 319 (2018).
[26] Z. L. Hussain, R. S. Fyath, Optik **251**, 168449 (2022).
[27] H. Li, T. Huang, L. Lu, Z. Hu, B. Yu, Opt. Laser Technol. **145**, 107465 (2022).
[28] J. Xiong, S.-T. Wu, Opt. Express **28**(24), 35960 (2020).
[29] X. Shi, B. Wang, Z. Cui, J. Li, H. Zhan, Indian J. Phys. **99**(5), 1891 (2025).
[30] A. Iguchi, K. Morimoto, Y. Tsuji, IEEE Photon. Technol. Lett. **33**(14), 707 (2021).
[31] K. Wang, T. Cui, L. Qian, Opt. Eng. **60**(7), 075102 (2021).
[32] B. Gong, H. Wen, H. Li, IEEE Photon. J. **12**(2), 6500208 (2020).
[33] Z. Lin, B. Wang, K. Wen, Opt. Commun. **505**, 127499 (2022).
[34] K. Han, C.-H. Chang, Nanomaterials **4**(1), 87 (2014).
[35] Y. Chen, S. Zhang, Y. Tian, C. Li, W. Huang, Y. Liu, Y. Jin, B. Fang, Z. Hong, X. Jing, Opto-Electron Adv. **7**(8), 240095 (2024).
[36] L. Liu, B. Wang, Z. Cui, H. Zhan, J. Li, Appl. Phys. B **130**, 32 (2024).
[37] X. Huang, B. Wang, Phys. Scr. **99**, 065569 (2024).
[38] T. Hou, Y. Ge, S. Xue, H. Chen, Front. Phys. **19**(3), 32201 (2024).
[39] J. Feng, C. Zhou, J. Zheng, B. Wang, Opt. Commun. **281**(21), 5298 (2008).
[40] H. Cao, C. Zhou, J. Feng, P. Lv, J. Ma, Opt. Commun. **283**(21), 4271 (2010).
[41] X. Ma, Y. Li, Y. Lu, J. Han, X. Zhang, W. Zhang, Front. Phys. **8**, 580781 (2020).
[42] H. Zou, B. Wang, J. Electromagn. Waves Appl. **37**(17), 1435 (2023).
[43] G. Liang, B. Wang, J. Li, H. Zhan, Z. Cui, Opt. Commun. **565**, 130654 (2024).
[44] X. Zhu, B. Wang, J. Li, X. Wang, H. Zou, L. Liu, L. Huang, X. Yang, W. Yu, J. Huang, Optoelectron. Adv. Mat. **16**(9-10), 407 (2022).
[45] C. Fu, B. Wang, J. Fang, K. Wen, Z. Meng, Q. Wang, Z. Nie, X. Xing, L. Chen, L. Lei, J. Zhou, Optoelectron. Adv. Mat. **14**(7-8), 297 (2020).
[46] F. Gong, R. Qin, K. Yang, Q. Ren, G. Yang, Infrared Phys. Technol. **146**, 105763 (2025).
[47] S. Huang, Z. Peng, S. Rui, R. Zhang, R.-T. Wen, X. Cheng, L. Guo, Rev. Sci. Instrum. **93**, 125112 (2022).

*Corresponding author: wangb_wsx@yeah.net